Chemical Science

ROYAL SOCIETY OF CHEMISTRY

EDGE ARTICLE

View Article Online
View Journal | View Issue

Cite this: *Chem. Sci.*, 2024, **15**, 6949

All publication charges for this article have been paid for by the Royal Society of Chemistry

Design enhancement in hydroxide ion conductivity of viologen–bakelite organic frameworks for a flexible rechargeable zinc–air battery†

Deepak Rase,[ab] Narugopal Manna,[ab] Rinku Kushwaha,[ab] Chitvan Jain,[ab] Himan Dev Singh,[ab] Pragalbh Shekhar,[ab] Piyush Singh,[ab] Yashraj Kumar Singh[a] and Ramanathan Vaidhyanathan *[abc]

Quasi-solid-state rechargeable zinc–air batteries (ZABs) are suitable for the generation of portable clean energy due to their high energy and power density, safety, and cost-effectiveness. Compared to the typical alkaline aqueous electrolyte in a ZAB, polymer or gel-based electrolytes can suppress the dissolution of zinc, preventing the precipitation of undesirable irreversible zinc compounds. Their low electronic conductivity minimizes zinc dendrite formation. However, gel electrolytes suffer from capacity fade due to the loss of the volatile solvent, failing to deliver high-energy and high-power ZABs. Consequently, developing polymers with high hydroxide ion conductivity and chemical durability is paramount. We report cationic C–C bonded robust polymers with stoichiometrically controlled mobile hydroxide ions as solid-state hydroxide ion transporters. To boot, we increased the viologen-hydroxide-ion concentration through "by-design" monomers. The polymers constructed with these designer monomers exhibit a commensurate increase in their ionic conductivity. The polymer prepared with 4 OH^- ion-containing monomer was superior to the one with 3 OH^-. The conductivity increases from 7.30×10^{-4} S cm^{-1} (30 °C) to 2.96×10^{-3} S cm^{-1} (30 °C) at 95% RH for IISERP-POF12_OH (**2_OH**) and IISERP-POF13_OH (**3_OH**), respectively. A rechargeable ZAB (RZAB) constructed using **3_OH@PVA** (polyvinyl alcohol) as the electrolyte membrane and Pt/C + RuO_2 catalyst delivers a power density of 158 mW cm^{-2}. In comparison, RZABs with a PVA interlayer provided only 72 mW cm^{-2}. Notably, the device suffered an initial charge–discharge voltage gap of merely 0.55 V at 10 mA cm^{-2}, which increased by only 2 mV after 50 hours of running. The battery operated at 10 mA cm^{-2} and worked steadily for 67 hours. We accomplished a flexible and rechargeable zinc–air battery (F-RZAB) exhibiting a maximum power density of 79 mW cm^{-2}. This demonstration of a cationic viologen–bakelite polymer-based flexible secondary ZAB with versatile stochiometric hydroxide-ion tunability marks an important achievement in hydroxide-ion conducting solid-state electrolyte development.

Received 7th January 2024
Accepted 24th March 2024

DOI: 10.1039/d4sc00121d

rsc.li/chemical-science

Introduction

Rechargeable zinc–air batteries (RZABs) represent a promising candidate for the development of flexible energy storage solutions.[1–14] This potential is rooted in their uncomplicated architecture, capacity to be modeled into diverse shapes, environment-friendly attributes, cost-effectiveness, and high energy and power density.[15–17] Traditionally, a battery having an alkaline electrolyte with a zinc anode is desirable due to the inherent electrochemical reversibility and fast kinetics (*e.g.*, low overpotential).[18,19] However, highly alkaline electrolytes cause zinc corrosion, shape changes, dendrite growth, precipitation of insoluble carbonates, electrolyte evaporation, and hydrogen evolution—all of which contribute to performance decay.[20–22] Rendering the ZAB as a solid-state battery solves many of these issues.[3,4,7,10,17,23] A major obstacle to integrating flexible designs for ZABs is the lack of appropriate solid electrolytes that can conduct hydroxide ions (OH^-) while being flexible. Alongside electrode kinetics, the efficient movement of hydroxide ions across the electrolyte significantly influences ZAB efficiency.[16,24] Although there is a recent surge in the investigation of hydroxide-ion conducting polymers for energy storage, they are aimed mostly for use as supercapacitor electrolytes and fuel cell membranes,[25–32] to our knowledge, there is only one report on their utilization in ZABs.[33] However, there is no evidence that

[a]*Department of Chemistry, Indian Institute of Science Education and Research, Dr Homi Bhabha Road, Pashan, Pune 411008, India. E-mail: vaidhya@iiserpune.ac.in*

[b]*Centre for Energy Science, Indian Institute of Science Education and Research, Dr Homi Bhabha Road, Pashan, Pune 411008, India*

[c]*The Centre of Excellence for Carbon Capture and Removal, Svante Incorporation, 8800 Glenlyon Pkwy, Burnaby, British Columbia, V5J 5K3, Canada*

† Electronic supplementary information (ESI) available. See DOI: https://doi.org/10.1039/d4sc00121d

these porous hydroxide-ion conducting polymer electrolytes can support a RZAB.

Polymeric membranes, which possess an inherent ability to facilitate OH^- ion conduction, are commonly referred to as anion exchange polymer electrolyte membranes (AEPEMs). These are distinguished by the presence of positively charged functional groups, such as quaternary nitrogen or imidazole groups and some hydrogen-bonding moieties integrated into the polymer chain.[30,34–36] These functional groups play a crucial role in creating interconnected nanochannels and enabling the selective conduction of anions *via* optimal electrostatic interactions; additionally, they cooperate very well with water within AEPEM networks.[37] However, their archetypal 1-D chain structure cannot avoid potential swelling, and if they are electronically conductive, it promotes Zn-dendrimer growth. High structural flexibility and porosity can promote the undesired passage of zincate ions through their pores.[38,39] These drawbacks underscore the need for alternative approaches in ZAB design and separator technology. Furthermore, considering that ZABs are designed to be cost-effective energy storage solutions, using expensive commercial AEPEM membranes is not an ideal approach. Consequently, there is a compelling need to engineer cost-effective AEPEMs.

Among polymer electrolytes and gel polymer electrolytes reported, poly(ethylene oxide) (PEO)[40,41] or PVDF-based systems,[42,43] as well as their combinations with various zinc salts, are the most studied for use in ZABs.[44] Polymer electrolytes, such as PEO, show poor ionic conductivity due to their semicrystalline nature. To attain high ionic conductivity, these polymers require the use of organic solvents, such as propylene carbonate (PC), ethylene carbonate (EC), and dimethylsulfoxide (DMSO).[42,43,45] Despite having acceptable ionic conductivity, such organic solvents are inapplicable for open systems, such as secondary zinc–air systems, due to their volatility.[46] Nevertheless, PVA has proven to be an excellent choice for flexible electrolyte preparation due to its hydrophilic nature and film-forming capabilities.[35,47–50] We decided to exploit these advantageous features of PVA by integrating it with a superior hydroxide ion-conducting polymer in an aqueous system.

To this end, robust C–C bonded cross-linked polymers capable of conducting hydroxide ions in humid environments became our target RZAB electrolyte material. Their amorphous nature and low electronic conductivity help minimize zinc-dendrite formation and their microporous structure is expected to favour selective conduction of hydroxide ions, while the organic framework can enable them to be a component of a flexible battery. They generally do not swell under aqueous conditions, hence as solid electrolytes, they will adhere to the electrode as its volume increases or reduces during charging and discharging, respectively.[51,52] Thus, in this study, a thin hydroxide ion-conducting solid-state separator coupled with an electrolyte has been devised for use in ZABs by a combination of cationic polymer with PVA through simple solution processing.

Inspired by the versatility of viologen chemistry[53,54] earlier we showed how viologen–bakelite polymers can be manipulated to have stoichiometrically loaded mobile hydroxide ions that render them superior quasi-solid electrolytes for primary zinc–air battery.[32,33] Following this, with the rapidly surging interest in secondary or rechargeable batteries, we realized the paramount need for demonstrating the potential of this hydroxide ion-conducting cationic polymer in the more challenging target of secondary zinc air battery where its compatibility demands increase.[55–57] Specifically, a hydroxide ion-exchanged POF was integrated with PVA to form a solid-state separator-cum-electrolyte for zinc–air battery applications. Moreover, considering that the monomeric building unit of these polymers can be tuned to have a systematically increased number of hydroxide ions per unit, we successfully verified that this stoichiometric control can be translated to enhanced hydroxide ion conductivity. Our demonstration of high-power density and running life for the proposed viologen–bakelite electrolyte-based RZAB creates numerous possibilities.

Results and discussion

Synthesis and characterisation of IISERP-POF12 (2) and IISERP-POF13 (3)

The synthesis of two novel polymers, IISERP-POF12 (**2**) and IISERP-POF13 (**3**), from the monomers and their conversion into **2_OH** and **3_OH** after the exchange of Br^- with OH^- ions is illustrated in Scheme 1. The details for synthesizing the catalyst are presented in the Experimental section of the ESI.† Briefly, the solvothermal reaction between 0.2 mmol phenolic compound and 0.2 (for **2**)–0.15 (for **3**) mmol viologen aldehyde in a mixture of 3 mL of THF and 3 mL of 1,4-dioxane at 200 °C for 72 h yielded the polymer as a brown-colored precipitate which was sequentially washed with DMF, THF, MeOH and finally, acetone. This powder was insoluble even in boiling DMF; hence, a Soxhlet wash was performed to remove

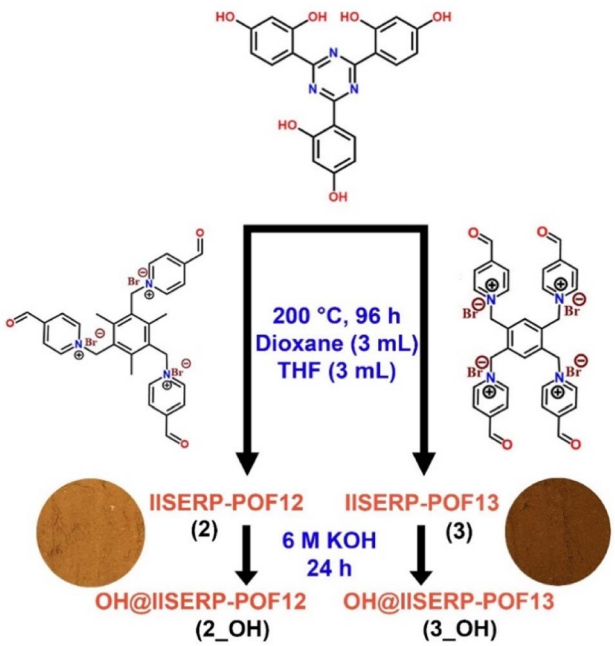

Scheme 1 Synthetic procedure of 2_OH and 3_OH. Circular insets show the photographic images of compounds 2 and 3.

unwanted oligomers, but none were observed. These as-made halogenated polymers **2** or **3** (100 mg) were converted to the hydroxide-ion-based polymer by exchanging the extra-framework guest halide ions for hydroxide ions using a KOH solution. A yield of ~85–89% was achieved for both the polymers. Note that we named our earlier hydroxide ion-conducting polymer from this family **1_OH**.[33]

There is evidence of Bakelite-type coupling between triazine-resorcinol and viologen-based bipyridinium aldehyde according to analysis of ^{13}C cross-polarisation (CP) magic angle spinning (MAS) solid-state nuclear magnetic resonance (NMR) (Fig. 1a and b). The coupling between an aldehyde and unsubstituted sites on phloroglucinol rings leads to a distinctive aliphatic peak for the C–C bond at 29 and 28 ppm for **2** and **3**, respectively. It is followed by other characteristic peaks from aromatic groups, such as triazine, at around 195 ppm for **2** and 191 ppm for **3**; aromatic peaks for a viologen-based unit are present at around 142 ppm and 143 ppm for **2** and **3**, respectively. The aliphatic peaks for building blocks around 69 ppm and 61 ppm were intact upon the formation of **2** and **3** (Fig. 1a and b).[58,59] While this shows that polymerization occurred, we recorded the NMR spectra of the material after boiling it in a THF + DMF mixture and later soaking it over 24 h in a 6 M KOH solution to exchange the Br^- with OH^- ions. The characteristic peaks were still equally intense and situated at similar chemical shifts. For electrolyte applications, the exceptional chemical stability and functional group integrity of the polymer, especially when subjected to harsh treatments, are highly desirable (Fig. 1a and b). Fig. 1c and d show the comparative FTIR spectrum of aldehyde monomers, *i.e.*, tri and tetra aldehyde, as-synthesized cationic polymers (**2** and **3**), their hydroxide exchanged forms: **2_OH**, and **3_OH**. The increase in intensity for C–H (2890 cm^{-1}) clarified that the C–C bond between phenolic and aldehyde moieties had formed, as evidenced by the elimination of C=O (1690 cm^{-1}) from the monomers upon polymerization. Additionally, C=N (1620 cm^{-1}) ensures the integrity of the building blocks in **2**, **2_OH**, **3**, and **3_OH**, respectively (Fig. 1c and d). These are highly cross-linked high-molecular-weight polymers that are insoluble even in boiling solvents (*e.g.*, glycol, DMF, and DMSO); hence, we could not use methods, such as gel permeation chromatography in our characterizations.

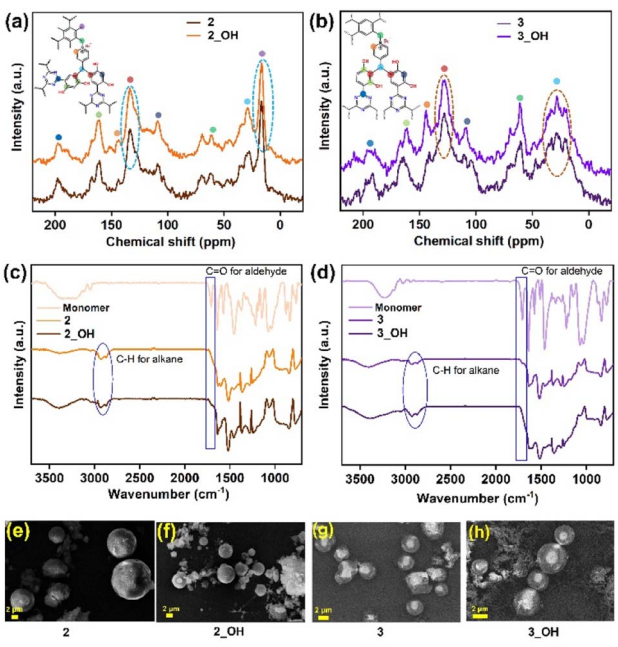

Fig. 1 (a) ^{13}C-CPMAS spectra of **2** and **2_OH**; (b) **3** and **3_OH**; (c) FTIR spectra of Aldehyde monomers, **2**, and **2_OH**; (d) **3**, and **3_OH**; (e and f) FESEM images of **2** and **2_OH**; (g and h) FESEM images of **3** and **3_OH**.

Field emission scanning electron microscopy (FESEM) and high-resolution transmission electron microscopy (HRTEM) images of **2** and **3** (Fig. 1e and g) show that polymer particles are agglomerated or intergrown microspheres with sizes ranging from 500 nm to 5 μm (Fig. S1, S3, S6 and S8, ESI†). Fig. 1f and h show that even after treatment of **2** and **3** with a 6 M KOH solution to make **2_OH** and **3_OH**, respectively, there was no deformation in the shape of these microspheres (Fig. 1f and h and Fig. S2 and S4, ESI†). This shows that their texture remained stable in the corrosive environment. Thus, **2_OH** and **3_OH** were well suited to operate under highly concentrated alkaline conditions that are necessitated by ZABs. The energy dispersive X-ray (EDX) analysis shows the systematic increment in the atomic percentage of the Br^- ions from **1** (ref. 33) to **3**. It shows the presence of excess Br^- ions available for the exchange with the OH^- ions (Fig. S5, ESI†). Moreover, the colour difference in **2** (brown) and **3** (dark brown) echoes the presence of a higher amount of the Br^- ions (Scheme 1).

High-resolution transmission electron microscopy (HRTEM) images unveiled that the spherical balls in **2** and **3** (Fig. S6 and S8, ESI†) are connected in a continuous manner, which can support ionic transport across grains and spheres. We noticed no changes in the surface diameter of **2_OH** and **3_OH** spheres during OH^- ion exchange, which further demonstrated the chemical stability of the polymers (Fig. S7 and S9, ESI†). However, the elemental mapping of **2** and **3** (Fig. S6 and S8, ESI†) reveals the presence of the Br^- ions, which significantly lowered when exchanged with OH^-. The presence of K^+ traces demonstrates that the exchange in **2_OH** and **3_OH** was successful (Fig. S7 and S9, ESI†).

Thermogravimetric analysis displayed that frameworks of **2** and **3** are stable up to 280 °C. We associate this with the strong C–C bond between the monomers, resembling the bonds in Bakelite (Fig. S10, ESI†). The cationic polymers treated with 6 M KOH, *i.e.*, **2_OH** and **3_OH**, display similar TGA profiles (Fig. S10, ESI†) and exhibit no effect of harsh alkaline conditions on their thermal stabilities.

The contact angle measurements on the surface of freshly synthesized halogen-containing polymer powders, labelled as **2** and **3**, indicated a super-hydrophobic nature (Fig. S11, ESI†). However, **2_OH** and **3_OH** prepared by exchanging the halogen for hydroxide ions in an aqueous alkaline medium resulted in hydrophilic powders (Fig. S12, ESI†). This change in surface wettability positively influences the interaction of materials with electrolytes. We investigated molecular porosity using

water sorption isotherms. The water adsorption isotherms for **2**, **3**, **2_OH**, and **3_OH** were almost identical, indicating that the pore environment and structure had not undergone significant changes; however, the water capacity of **2_OH** and **3_OH** was higher than that of **2** and **3**, demonstrating the improved intrinsic wettability of the former. Thus, materials with Br^- containing frameworks are nearly super-hydrophobic ($140 \pm 3°$) and become significantly hydrophilic when bromides are replaced by the OH^- ions (Fig. S13a, ESI†). Notably, neither a significant change in density nor a detectable swelling of the polymer occurred (Fig. S13b–f, ESI†).

Electrochemical studies

Electrochemical impedance analysis was performed in the 10^6 to 0.1 Hz frequency range with an AC amplitude of 10 mV using a Solartron impedance analyzer. The densely pressed pellet of **2**, **3**, **2_OH**, and **3_OH** were employed to evaluate the intrinsic conductivity measurements of polymers. The impedance was recorded at variable temperatures (30 °C to 80 °C) and relative humidities (30% to 95%) (Fig. S14 to S17, ESI†). The as-synthesized polymers, **2** and **3**, displayed extremely low Br^- ion-mediated ionic conductivity values (Fig. S14, ESI†). It is expected that the Br^- ions are heavier and will be even less effective for a hydrogen-bond-assisted Grotthuss-type movement. The conductivity significantly increased after exchange with hydroxide ions, and the highest values were achieved for a range of temperatures at a constant relative humidity of 95%. The OH^- ion conductivity value increase from 7.30×10^{-4} S cm^{-1} (30 °C) to 1.53×10^{-2} S cm^{-1} (80 °C) and 2.96×10^{-3} S cm^{-1} (30 °C) to 4.88×10^{-2} S cm^{-1} (80 °C) for **2_OH** and **3_OH**, respectively (Fig. 2a, S15a, b and Table S1, ESI†).

The equivalent circuit was fitted for all Nyquist curves using the Zview-4 software. The comparison of the most promising Nyquist plots (30 °C, 95% RH) for **2_OH** *vs.* **3_OH** (Fig. 2a) suggests that the series and charge-transfer resistance types are substantially higher for **2_OH** ($R_1 = 140.1\ \Omega$, $R_2 = 281.3\ \Omega$) compared to **3_OH** ($R_1 = 35.4\ \Omega$, $R_2 = 61.6\ \Omega$). However, **2_OH** and **3_OH** exhibit typical semi-infinite linear diffusion, *i.e.*, diffusion in one dimension that is only constrained by a substantial planar electrode on one side (at a 45° angle to the z'-axis). We confirmed the need for a CPE component by measuring the CV of **2_OH** and **3_OH**, which showed that the capacitive behaviour was present in the fitted equivalent circuit (Fig. S15c and S18, ESI†). A pseudocapacitive behaviour anticipated for the polymer with the porous structure is shown by a CPE-P value close to 0.5 for both pellets. In our scenario, hydroxide ions move through pathways created by the presence of hydroxyl groups and triazine. These pathways can potentially facilitate the formation of hydrogen bonds, contributing to the Grotthuss mechanism. However, concurrently applying an AC potential can generate sufficient force to induce vehicular motion.

Furthermore, we investigated AC-impedance by varying the temperature (30 °C to 80 °C) to examine the humidity-dependent conductivity of **2_OH** and **3_OH** (Fig. 2b, S16 and S17, ESI†). Comparative heatmaps of **2_OH** and **3_OH** show that conductivities of the polymers range from 10^{-8} S cm^{-1} (30% RH at 30 °C) to 10^{-2} S cm^{-1} (95% RH at 80 °C). A steady rise in

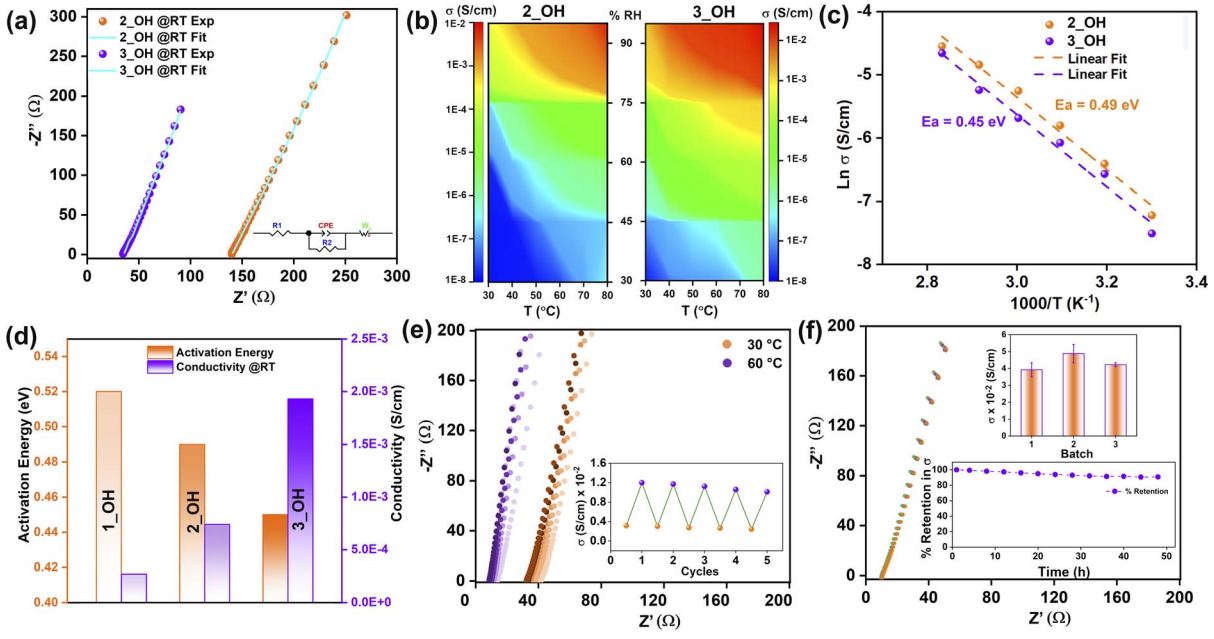

Fig. 2 (a) Measurement of hydroxyl ion conductivity for IISER-COF; (b) investigation of comparable activation energy of **2_OH** and **3_OH** based membrane; (c) construction of Arrhenius plots to investigate the activation energies of **2_OH** and **3_OH** based membrane; (d) comparable activation energy and conductivity of **1_OH**, **2_OH**, and **3_OH**; (e) OH^- ion conductivity measurements at varying temperatures (inset shows the change in the conductivity with temperature in various cycles); (f) comparison of Nyquist plots for **3_OH**, (top inset image shows the hydroxyl ions conductivity with POF from a different batch of synthesis, inset at the bottom shows the retention of hydroxyl ions conductivity with time).

conductivity values was seen up to 80% RH as the temperature was elevated, but after that, both the polymers exhibited a sudden increase in conductivity (where the area on the plot changes from green to yellowish orange). Particularly, **3_OH** has a higher conductivity value than **2_OH** even at lower temperatures, especially above 80% RH (the wider area covered by the red-coloured zone).

Increasing hydroxide ion conductivity with increasing temperature implies a lowering of the activation energy. In contrast, increased conductivity with increasing humidity means that water could play a crucial role *via* hydrogen bonding. This takes into account the fact that the polymer lacks a crystalline structure with well-organized pores and that its electronic conductivity is constrained at longer-length scales.[60] To examine the electronic conductivity of **2_OH** and **3_OH**, linear sweep voltammetry (LSV) was used at a scan rate of 10 mV s^{-1} across a potential window of −1 to 1 V (Fig. S19, ESI†). The conductivity observed for **2_OH** and **3_OH** is primarily ionic, likely due to the OH^- ions, as evidenced by their minimal electronic conductivity.

Activation energies of 0.49 eV and 0.45 eV for **2_OH** and **3_OH** are obtained when the Arrhenius equation is fitted to temperature-dependent impedance data (Fig. 2c), which points to the occurrence of the Grotthuss diffusion process.[61] The reported activation energy for hydroxide ions in various nanoporous materials is comparable to observed activation energies.[62]

It must be noted that when comparing our results to those of earlier research, the polymers show a gradual increase in hydroxide ion conductivity from **1_OH**[33] to **3_OH** (Fig. 2d and Table S1, ESI†)., which was anticipated, given the systematic increment in intrinsic hydroxide ion concentrations. The activation energy obtained from **1_OH** to **3_OH** is almost the same since the structural environments of the polymers remain similar among all three cases. Using the Z' *vs.* $\omega^{-1/2}$ plot, we computed the diffusion coefficient for hydroxide ions inside the cationic polymer framework. The low-frequency spectrum in the impedance plot produced distinctive linear fits (Fig. S20, ESI†) from which the diffusion coefficients at 80 °C and 95% relative humidity were calculated to be 3.61×10^{-5} cm^2 s^{-1} (**2_OH**) and 3.71×10^{-5} cm^2 s^{-1} (**3_OH**). As the temperature rose, the diffusion coefficient increased systematically (Fig. S20, ESI†). The calculated diffusion coefficients at 80 °C and 95% relative humidity agreed well with values published in the earlier publication 2.9×10^{-5} cm^2 s^{-1} (**1_OH**).

The best-performing polymer, *i.e.*, **3_OH**, was tested for temperature-dependent cycling stability in an 8 hours cycle ranging between 30 °C and 60 °C at 95% relative humidity (Fig. 2e). The cycling demonstrated excellent conductivity retention when temperature was varied between 30 °C and 60 °C. We also measured conductivity for various batches of **3_OH**, and the results are in the same order (Fig. 2f inset-top). Additionally, for more than 50 hours, outstanding time-dependent stability of up to 95% was demonstrated for conductivity (Fig. 2f inset-bottom). Regarding post-impedance characterization, the polymers **2_OH** and **3_OH** showed excellent chemical and structural integrity. The SS-NMR demonstrates retention of all peaks from pristine polymers (Fig. S21, ESI†), and the surface morphology is also intact in FESEM images (Fig. S22 and S23, ESI†).

The remarkable robust nature of the polymers makes them apt candidates for charge storage applications in harsh alkaline conditions like zinc–air batteries. We explored the application potential of exceptional hydroxide ion-conducting viologen polymer **3_OH** as a solid-state electrolyte in a zinc–air battery. A thin, flexible, and stable membrane is developed by blending **3_OH** and polyvinyl alcohol (PVA) in a 1 : 1 ratio (**3_OH@PVA**), as shown in Fig. 3a. Photographs shown in red circles are images of the membrane at different stages. According to the FESEM images (Fig. 3a, highlighted in a yellow ring, and Fig. S24a, ESI†), membranes with a uniform surface would considerably assist in creating an interface between the electrode and electrolyte. The ultra-thin membrane with a thickness of just 277 μm is seen in the cross-sectional FESEM images. It contains uniformly distributed polymer spheres, which assist in speeding up ion transport *via* a shorter path (Fig. S24d and e, ESI†). The analysis of AFM images and amplitude roughness parameters indicates that the electrolyte membrane exhibits satisfactory flatness. The consistent mean surface roughness (Sa) values, ranging from 177 nm to 268 nm across different samples, demonstrate that the membrane maintains a consistent level of flatness (Fig. S25 and Table S2, ESI†). Measurements of the conductivity of the membrane revealed a significantly promising hydroxide ion conductivity of 4.78×10^{-3} S cm^{-1} at room temperature (25 °C) in the presence of 95% humidity. The conductivity increased, reaching a maximum of 2.53×10^{-2} S cm^{-1}, when the temperature was changed from room temperature to 80 °C (Fig. 3b). Along with superior ionic conductivity, the membrane exhibits excellent flexibility on bending, stretching and crumbling (Fig. 3c–f). Minimal change in membrane thickness was observed, when the membrane was

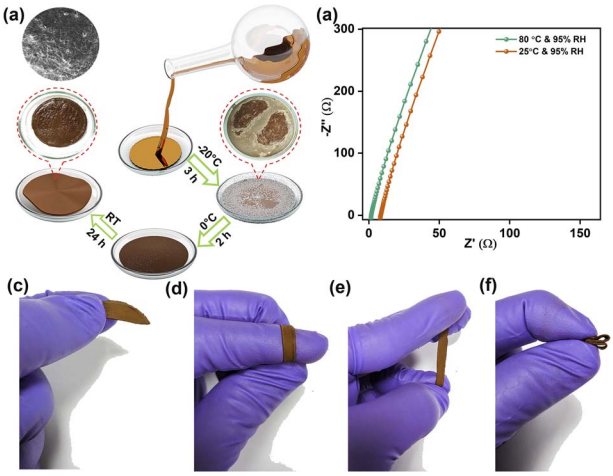

Fig. 3 (a) Schematic of the preparation of thin, flexible OH^- ion conducting membrane; (b) comparison of Nyquist plots for **3_OH@PVA** at various temperatures and 95% humidity; (c–f) digital photograph of the synthesized membrane and their flexibility at different bending modes.

immersed in an alkali solution for 12 hours indicating excellent stability in alkaline conditions (Table S3, ESI†).

Quasi solid-state electrolyte in ZAB

To assess the suitability of **3_OH@PVA** used as a quasi-solid-state electrolyte for rechargeable zinc–air battery (ZAB) applications, a conventional ZAB cell was assembled (Fig. 4a and S26, ESI†). In this cell configuration, **3_OH@PVA** served as the quasi-solid-state electrolyte, while Pt/C–RuO_2 was employed as the air-cathode, and the anode consisted of zinc paste (comprising Zn powder mixed with a solution of 3 M KOH) and 0.2 M $Zn(OAc)_2$. As depicted in Fig. 4a, the ZAB configuration includes the use of an ORR catalyst-coated gas carbon diffusion layer (GDL) as the cathode, zinc powder as the anode, and **3_OH@PVA** as the

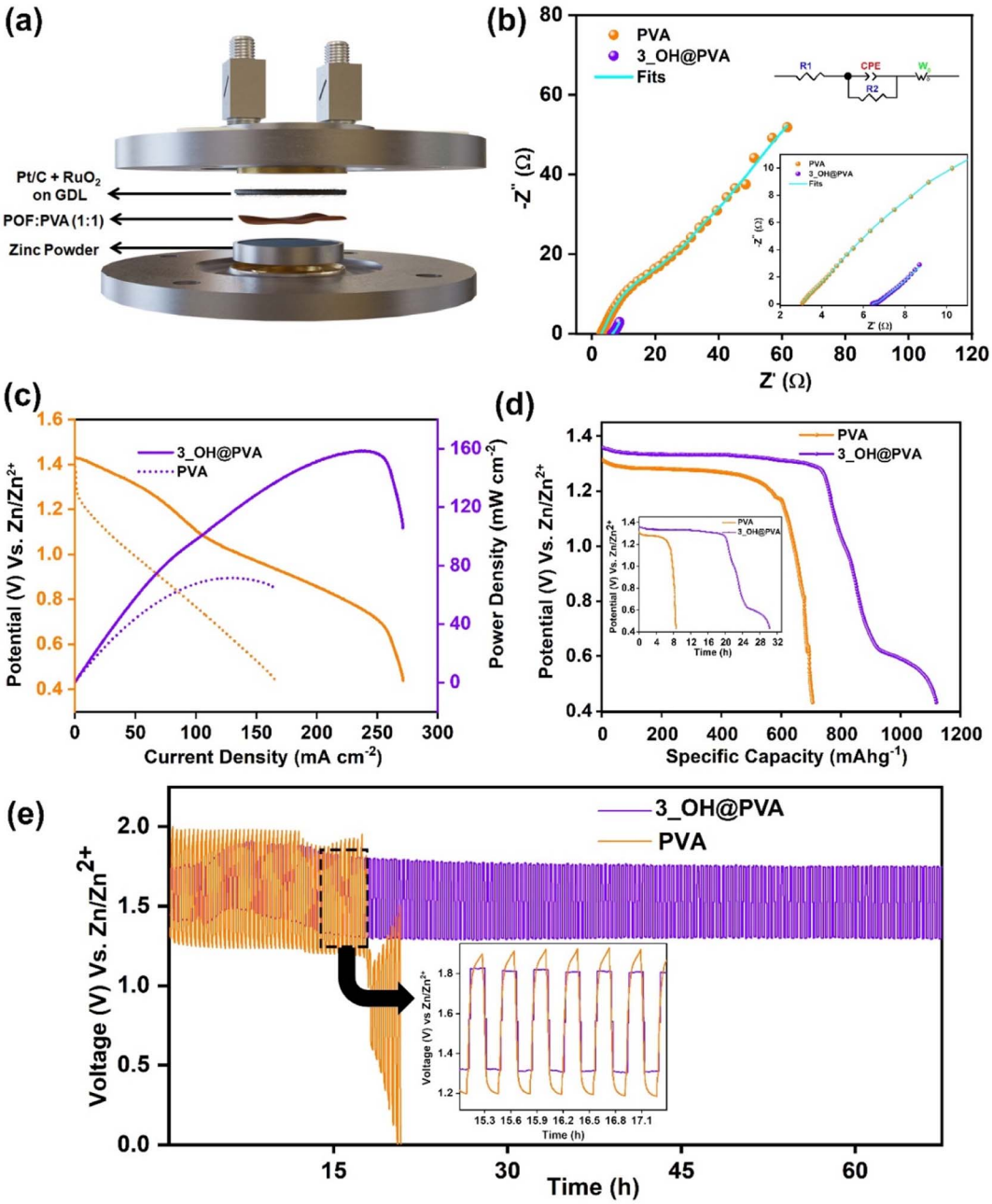

Fig. 4 (a) Schematic representation of the quasi-solid-state RZAB: where the cathode catalyst loading is set at 1.0 mg cm^{-2}, the anode employs zinc powder, and the separator consists of a membrane; (b) Nyquist plots from electrochemical impedance spectroscopy (EIS) analysis recorded for RZAB cells at the open-circuit voltage (OCV) condition, along with the corresponding equivalent circuit model fit; (c) polarization plots were generated for ZABs produced using Pt/C + RuO_2 as air electrodes, illustrating their electrochemical performance; (d) galvanostatic discharge capacities of fabricated ZABs, normalized by the amount of zinc consumed during the discharge process; (e) long-term galvanostatic charge–discharge profiles of the ZABs employing Pt/C + RuO_2 as the cathode catalysts were monitored until the anodic zinc powder was completely consumed.

electrolyte. During ZAB operation, oxygen diffuses through the porous air cathode and undergoes reduction to form the hydroxide ions (OH^-), which subsequently migrate toward the anode through the electrolyte, facilitating the oxidation of zinc into its hydroxide or oxide forms. The electrons released during the zinc oxidation process flow through the external circuit, thereby establishing the flow of electric current. The open circuit voltage (OCV) setup of the cell was subjected to electrochemical impedance spectroscopy (EIS) analysis. The comparative Nyquist plots for PVA-based and **3_OH@PVA**-based membranes, along with the fit of an equivalent circuit model, are illustrated in Fig. 4b.

The performance of the system is comparable to previously reported ZAB systems in the literature (refer to Table S4, ESI†). The comparative analysis of steady-state cell polarization (Fig. 4c) reveals maximum power densities (P_{max}) of 72 mW cm^{-2} and 158 mW cm^{-2} for ZABs utilizing PVA and **3_OH@PVA** as membranes, respectively. Notably, the **3_OH@PVA**-based cell gradually improved its performance compared to the PVA-based counterpart, ultimately it outperformed the latter. This improvement can be attributed to the intrinsic advantages of **3_OH@PVA** membranes, particularly in terms of mass transport facilitated by the membrane and interface formation between the electrolytes. Furthermore, the superior performance of the **3_OH@PVA** membrane can be directly attributed to the improved ionic conductivity of the membrane an enhanced contact achieved at the electrode–electrolyte interface.

To determine the specific capacities of the prepared ZAB cell, the discharge process was carried out to a voltage of 1.38 V at a current density of 10 mA cm^{-2}. Moreover, the galvanostatic discharge curve, captured at a current density of 10 mA cm^{-2} (Fig. 4d), provides evidence of the durability of the ZAB system. It is noteworthy that discharge durations for ZABs utilizing **3_OH@PVA** and PVA as membranes are approximately 22 hours and 8 hours, respectively (Fig. 4d inset). The observed voltage decreases within the plateau region over the course of operation, which is likely attributable to side reactions occurring at the surface of the zinc powder, as indicated in prior studies. The calculated specific capacity, as illustrated in Fig. 4d, for the constructed zinc–air battery (ZAB) utilizing **3_OH@PVA** membrane as the separator-cum-electrolyte, amounts to approximately 742 mA h g_{Zn}^{-1}. In comparison, the ZAB system employing PVA as the separator-cum-electrolyte exhibits a specific capacity of around 579 mA h g_{Zn}^{-1}. The failure of RZAB (PVA-KOH) systems after 8 hours can be attributed to the rapid drying of the commercial and PVA-KOH membranes within the semi-open ZAB system configured for air-breathing. This drying phenomenon is a consequence of inferior electrolyte retention characteristics exhibited by the PVA-KOH membrane.

Furthermore, Fig. 4e displays galvanostatic charge–discharge curves recorded for cells operating at 10 mA cm^{-2}. The zinc–air battery (ZAB) fabrication using **3_OH@PVA** revealed a lower voltage difference (0.55 V) between charging and discharging compared to PVA-KOH (0.72 V). Over 67 hours of continuous charge–discharge cycles, the **3_OH@PVA** membrane-based cell showed a nominal increase of 0.02 V in the voltage difference. In contrast, the PVA-KOH-based system exhibited a rapid increase to 0.67 V within just 17 hours, leading to the termination of the test. Additionally, the inset image (Fig. 4e) of the magnified charge–discharge profile between 14 to 18 hours shows the symmetric plateau nature of the **3_OH@PVA** membrane-based RZAB, while the PVA-KOH cell displayed asymmetric behaviour. This difference reveals the better interface formation and water uptake capacity of **3_OH@PVA** compared to PVA-KOH which helps run charge–discharge devices for long durations.

In response to the growing interest in portable and flexible electronic devices, we designed and demonstrated a flexible and rechargeable zinc–air battery (F-RZAB) with a surface area of 2 × 2 cm^2. This innovative system utilized a catalyst-coated carbon cloth as the cathode, a **3_OH@PVA**-based membrane as the electrolyte, and a polished 0.10 mm thick zinc foil as the anode (Fig. 5a). A flexible solid-state ZAB was developed to demonstrate the practical usability of the as-prepared **3_OH@PVA** (Fig. 5a), resulting in a combined voltage of 1.386 V, as measured using a multimeter device (Fig. 5b). More information is provided in the ESI Section.† Without additional O_2 gas purging, the constructed solid-state battery delivers an OCV value of 1.38 V (Fig. 5b) in air. According to the polarisation study shown in Fig. 5c, the maximum power density was 79 mW cm^{-2}. The output voltage remained stable on bending the device at different angles (Fig. 5d–g), owing to the liquid-free nature of **3_OH@PVA**.

The flexibility of the device was assessed by monitoring its open-circuit voltage (OCV) at various bending angles (0°, 90°, and 180°). Remarkably, the system maintained a consistent OCV of approximately 1.40 V across these different bending angles (Fig. 5d). Fig. 5e–g shows the digital photographs of the flexible device from various angles.

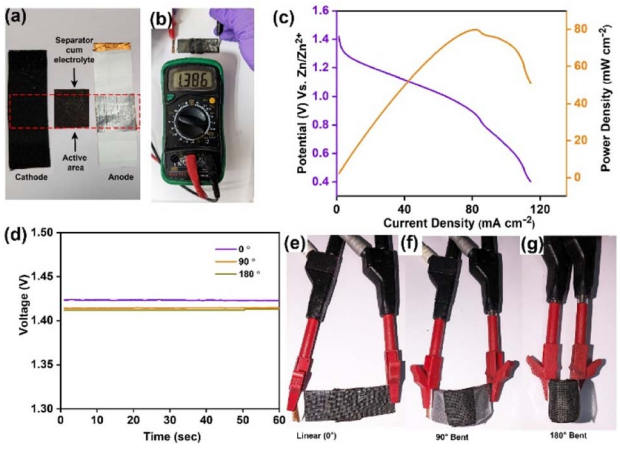

Fig. 5 (a) Components of F-RZABs showing cathode, anode and electrolyte; (b) digital photograph of F-RZAB and multimeter device respectively; (c) recording of the current (*I*)–voltage (*V*) polarization plot for F-RZAB; (d) comparative OCV acquired at different bending angles, illustrating the device flexibility; (e–g) digital photograph of the flexible device at various angles (0°, 90°, and 180°).

Post-battery characterizations

When used as a separator-cum-electrolyte in the ZAB, the stability of **3_OH@PVA** was examined. According to PXRD analysis, no ZnO characteristic peaks were observed for the cathode side, suggesting that dendrite growth during battery measurements did not cause membrane tearing (Fig. S27, ESI†).

The neat PVA membrane displayed a few tiny fractures during battery measurements (Fig. S28b–d, ESI†). In contrast, the membrane in the case of **3_OH@PVA** is stable and undamaged with uniformly distributed spherical polymer particles (Fig. S29e and f, ESI†), just like initial condition of the membrane (Fig. S24a, ESI†). Additionally, the thickness of **3_OH@PVA** dropped from 277 μm to 177 μm (Fig. S28d, ESI†) on post-battery characterization, which may be attributed to pressure applied during battery packing.

Conclusions

A new strategy for the POF-based membrane has been developed, involving controlled polymerization initiated from a pre-admitted and infiltrated precursor. This POF-based membrane shows robust OH^- ion conductivity of 2.53×10^{-2} S cm^{-1}. Additionally, it features desirable attributes, such as high electrolyte uptake and retention capacity. The rechargeable ZAB assembled through a POF-based membrane in quasi-solid-state and flexible device applications shows favourable enhancements in the performance of RZABs. The performance evaluation of the rechargeable zinc–air battery (RZAB) containing a POF-membrane, in conjunction with the Pt/C–RuO_2 catalyst-coated air-cathode, revealed a peak power density of 158 mW cm^{-2} at a current density of 246 mA cm^{-2} and specific capacity of 742 mA h g^{-1}. This was accompanied by promising charging/discharging characteristics. To validate the flexibility of the system, the POF membrane was integrated with a thin Zn foil as the anode and a Pt/C–RuO_2 catalyst-coated carbon cloth featuring the cathode. F-RZAB delivered an OCV value of 1.38 V in air, and its maximum power density was 79 mW cm^{-2}. Remarkably, the system maintained a consistent OCV of approximately 1.40 V across the different bending angles. Beyond the realm of metal–air batteries, the outcomes of this study and strategies employed here hold promise as effective practical solutions that can offer technological benefits in various electrochemical systems by enhancing performance in quasi-solid-state and flexible configurations.

Data availability

All experimental data is provided in the ESI.†

Author contributions

DR designed and synthesized the materials, carried out the characterization and property investigation experiments and drafted the manuscript. NM designed and helped with the electrochemical studies and data analysis and closely supervised the drafting of the first version of this manuscript. HDS and PS carried out the porosity characterization studies, while RK and CJ helped with the conductivity studies. RK assisted with membrane development. YKS worked on the ligand synthesis, aided with the synthesis of multiple batches of polymers and helped in membrane development. VR conceived the idea, supervised the work and drafted the manuscript.

Conflicts of interest

All authors have given approval to the final version of the manuscript. The authors declare no competing interests.

Acknowledgements

DR thanks IISER Pune for the financial support, and CJ thanks the University Grant Commission (UGC) for the fellowship. HDS and PS thank the Council of Scientific and Industrial Research (CSIR) for the fellowship, and RK thanks the Air Force Office of Scientific Research under Award Number FA2386-21-1-4022 for financial support. We thank the MHRD-FAST (MHRD Project 150 (F. No. 5-5/2014 TS-VII and F. No. 22-2/2016 TS-II/TC)) program and MHRD-STARS [STARS1/278] program for the research funding. The authors thank the Department of Science and Technology, GOI, for the Material for Energy Storage (DST/TMD/MES/2k17/103) program and the "DST-Nanomission under the Thematic Unit Program" (EMR/2016/003553). We acknowledge the Science and Engineering Research Board, GOI, (CRG/2021/008250).

References

1 J.-N. Liu, C.-X. Zhao, J. Wang, D. Ren, B.-Q. Li and Q. Zhang, *Energy Environ. Sci.*, 2022, **15**, 4542–4553.
2 T. Zhang, Y. Tang, S. Guo, X. Cao, A. Pan, G. Fang, J. Zhou and S. Liang, *Energy Environ. Sci.*, 2020, **13**, 4625–4665.
3 Q. Wang, S. Kaushik, X. Xiao and Q. Xu, *Chem. Soc. Rev.*, 2023, **52**, 6139–6190.
4 P. Tan, B. Chen, H. Xu, H. Zhang, W. Cai, M. Ni, M. Liu and Z. Shao, *Energy Environ. Sci.*, 2017, **10**, 2056–2080.
5 R. Kushwaha, C. Jain, P. Shekhar, D. Rase, R. Illathvalappil, D. Mekan, A. Camellus, C. P. Vinod and R. Vaidhyanathan, *Adv. Energy Mater.*, 2023, **13**, 2301049.
6 J. S. Lee, S. Tai Kim, R. Cao, N. S. Choi, M. Liu, K. T. Lee and J. Cho, *Adv. Energy Mater.*, 2011, **1**, 34–50.
7 P. Zhang, Z. Chen, N. Shang, K. Wang, Y. Zuo, M. Wei, H. Wang, D. Zhong and P. Pei, *Mater. Chem. Front.*, 2023, **7**, 3994–4018.
8 J. Fu, Z. P. Cano, M. G. Park, A. Yu, M. Fowler and Z. Chen, *Adv. Mater.*, 2017, **29**, 1604685.
9 S. S. Shinde, N. K. Wagh, C. H. Lee, D. H. Kim, S. H. Kim, H. D. Um, S. U. Lee and J. H. Lee, *Adv. Mater.*, 2023, **35**, 2303509.
10 Z. Farmani, M. A. Sedghamiz and M. R. Rahimpour, *Zinc Batteries: Basics, Developments, and Applications*, 2020, pp. 187–213.
11 A. M. Asiri and R. Boddula, *Zinc Batteries: Basics, Developments, and Applications*, John Wiley & Sons, 2020.

12 X. W. Lv, Z. Wang, Z. Lai, Y. Liu, T. Ma, J. Geng and Z. Y. Yuan, *Small*, 2023, 2306396.
13 S. Peng, *Zinc–Air Batteries: Fundamentals, Key Materials and Application*, Springer Nature, 2023.
14 N. Manna, S. K. Singh, M. Kurian, A. Torris and S. Kurungot, *ACS Appl. Energy Mater.*, 2022, **5**, 8756–8768.
15 Q. Liu, R. Liu, C. He, C. Xia, W. Guo, Z.-L. Xu and B. Y. Xia, *eScience*, 2022, **2**, 453–466.
16 A. R. Mainar, E. Iruin, L. C. Colmenares, A. Kvasha, I. De Meatza, M. Bengoechea, O. Leonet, I. Boyano, Z. Zhang and J. A. Blazquez, *J. Energy Storage*, 2018, **15**, 304–328.
17 M. Xu, D. Ivey, Z. Xie and W. Qu, *J. Power Sources*, 2015, **283**, 358–371.
18 C. Chakkaravarthy, A. A. Waheed and H. Udupa, *J. Power Sources*, 1981, **6**, 203–228.
19 R. Gilliam, J. Graydon, D. Kirk and S. Thorpe, *Int. J. Hydrogen Energy*, 2007, **32**, 359–364.
20 X. Liu, X. Fan, B. Liu, J. Ding, Y. Deng, X. Han, C. Zhong and W. Hu, *Adv. Mater.*, 2021, **33**, 2006461.
21 A. R. Mainar, O. Leonet, M. Bengoechea, I. Boyano, I. de Meatza, A. Kvasha, A. Guerfi and J. Alberto Blázquez, *Int. J. Energy Res.*, 2016, **40**, 1032–1049.
22 V. Verma, R. M. Chan, L. Jia Yang, S. Kumar, S. Sattayaporn, R. Chua, Y. Cai, P. Kidkhunthod, W. Manalastas Jr and M. Srinivasan, *Chem. Mater.*, 2021, **33**, 1330–1340.
23 Y. Wei, Y. Shi, Y. Chen, C. Xiao and S. Ding, *J. Mater. Chem. A*, 2021, **9**, 4415–4453.
24 X. Cai, L. Lai, J. Lin and Z. Shen, *Mater. Horiz.*, 2017, **4**, 945–976.
25 J. Li, J. Qiao and K. Lian, *Sustainable Energy Fuels*, 2017, **1**, 1580–1587.
26 C. Choi, K. Robert, G. Whang, P. Roussel, C. Lethien and B. Dunn, *Joule*, 2021, **5**, 2466–2478.
27 J. Li, J. Qiao and K. Lian, *Energy Storage Mater.*, 2020, **24**, 6–21.
28 O. D. Thomas, K. J. Soo, T. J. Peckham, M. P. Kulkarni and S. Holdcroft, *J. Am. Chem. Soc.*, 2012, **134**, 10753–10756.
29 W.-H. Lee, A. D. Mohanty and C. Bae, *ACS Macro Lett.*, 2015, **4**, 453–457.
30 F. Wang, D. Wang and Y. Nagao, *ChemSusChem*, 2021, **14**, 2694–2697.
31 J. Fan, S. Willdorf-Cohen, E. M. Schibli, Z. Paula, W. Li, T. J. Skalski, A. T. Sergeenko, A. Hohenadel, B. J. Frisken and E. Magliocca, *Nat. Commun.*, 2019, **10**, 2306.
32 F. Liu, H.-J. Chung and J. A. Elliott, *ACS Appl. Energy Mater.*, 2018, **1**, 1489–1495.
33 D. Rase, R. Illathvalappil, H. D. Singh, P. Shekhar, L. S. Leo, D. Chakraborty, S. Haldar, A. Shelke, T. G. Ajithkumar and R. Vaidhyanathan, *Nanoscale Horiz.*, 2023, **8**, 224–234.
34 R. Chen, X. Xu, S. Peng, J. Chen, D. Yu, C. Xiao, Y. Li, Y. Chen, X. Hu and M. Liu, *ACS Sustainable Chem. Eng.*, 2020, **8**, 11501–11511.
35 X. Zhong, Z. Zheng, J. Xu, X. Xiao, C. Sun, M. Zhang, J. Ma, B. Xu, K. Yu and X. Zhang, *Adv. Mater.*, 2023, **35**, 2209980.
36 M. Kurian, V. Vijayakumar, N. Manna, F. Kanheerampockil, S. Bhat and S. Kurungot, *J. Mater. Chem. A*, 2023, **11**, 14776–14787.
37 A. D. Easley, K. Mohanty and J. L. Lutkenhaus, *J. Mater. Chem. A*, 2023, **11**, 8783–8790.
38 M. T. Tsehaye, F. Alloin, C. Iojoiu, R. A. Tufa, D. Aili, P. Fischer and S. Velizarov, *J. Power Sources*, 2020, **475**, 228689.
39 R. K. Sankaralingam, S. Seshadri, J. Sunarso, A. I. Bhatt and A. Kapoor, *Mater. Today: Proc.*, 2022, **64**, 1649–1654.
40 W. Hagan, R. Latham, R. Linford and S. Vickers, *Solid State Ionics*, 1994, **70**, 666–669.
41 J. Fauvarque, S. Guinot, N. Bouzir, E. Salmon and J. Penneau, *Electrochim. Acta*, 1995, **40**, 2449–2453.
42 G. G. Kumar and S. Sampath, *Solid State Ionics*, 2003, **160**, 289–300.
43 G. G. Kumar and S. Sampath, *Polymer*, 2004, **45**, 2889–2895.
44 S. Ikeda, Y. Mori, Y. Furuhashi and H. Masuda, *Solid State Ionics*, 1999, **121**, 329–333.
45 A. Lewandowski and I. Majchrzak, *J. New Mater. Electrochem. Syst.*, 2001, **4**, 135–142.
46 H. Ye and J. J. Xu, *J. Power Sources*, 2007, **165**, 500–508.
47 Z.-X. Lin, Y.-T. Lu, C.-Y. Lai and C.-C. Hu, *J. New Mater. Electrochem. Syst.*, 2021, **168**, 100531.
48 E. García-Gaitán, D. Frattini, I. Ruiz de Larramendi, M. Martínez-Ibáñez, D. González, M. Armand and N. Ortiz-Vitoriano, *Batteries Supercaps*, 2023, **6**, e202200570.
49 X. Fan, R. Zhang, S. Sui, X. Liu, J. Liu, C. Shi, N. Zhao, C. Zhong and W. Hu, *Angew. Chem., Int. Ed.*, 2023, **62**, e202302640.
50 X. Fan, H. Wang, X. Liu, J. Liu, N. Zhao, C. Zhong, W. Hu and J. Lu, *Adv. Mater.*, 2023, **35**, 2209290.
51 G. Zhang, X. Cai, C. Li, J. Yao, W. Liu, C. Qiao, G. Li, Q. Wang and J. Han, *ACS Appl. Polym. Mater.*, 2023, **5**, 3622–3631.
52 S. K. Yadav, D. Deckenbach and J. J. Schneider, *Batteries*, 2022, **8**, 244.
53 Y. Zhang, Y.-P. Deng, J. Wang, Y. Jiang, G. Cui, L. Shui, A. Yu, X. Wang and Z. Chen, *Energy Storage Mater.*, 2021, **35**, 538–549.
54 H. Dou, M. Xu, Y. Zheng, Z. Li, G. Wen, Z. Zhang, L. Yang, Q. Ma, A. Yu and D. Luo, *Adv. Mater.*, 2022, **34**, 2110585.
55 M. Kathiresan, B. Ambrose, N. Angulakshmi, D. E. Mathew, D. Sujatha and A. M. Stephan, *J. Mater. Chem. A*, 2021, **9**, 27215–27233.
56 H. Nishide, *Green Chem.*, 2022, **24**, 4650–4679.
57 P. Gu, M. Zheng, Q. Zhao, X. Xiao, H. Xue and H. Pang, *J. Mater. Chem. A*, 2017, **5**, 7651–7666.
58 D. Crespy, M. Bozonnet and M. Meier, *Angew. Chem., Int. Ed.*, 2008, **47**, 3322–3328.
59 S. Haldar, D. Rase, P. Shekhar, C. Jain, C. P. Vinod, E. Zhang, L. Shupletsov, S. Kaskel and R. Vaidhyanathan, *Adv. Energy Mater.*, 2022, **12**, 2200754.
60 U. Tröltzsch and O. Kanoun, *Electrochim. Acta*, 2012, **75**, 347–356.
61 G. A. Luduena, T. D. Kühne and D. Sebastiani, *Chem. Mater.*, 2011, **23**, 1424–1429.
62 D. W. Kang, M. Kang, H. Yun, H. Park and C. S. Hong, *Adv. Funct. Mater.*, 2021, **31**, 2100083.